JACS
JOURNAL OF THE AMERICAN CHEMICAL SOCIETY
Article
pubs.acs.org/JACS

Enhanced Thermoelectric Properties in the Counter-Doped SnTe System with Strained Endotaxial SrTe

Li-Dong Zhao,*[,†] Xiao Zhang,[†] Haijun Wu,[‡,§,#] Gangjian Tan,[⊥] Yanling Pei,[†] Yu Xiao,[†] Cheng Chang,[†] Di Wu,[‡,§] Hang Chi,[∥] Lei Zheng,[†] Shengkai Gong,[†] Ctirad Uher,[∥] Jiaqing He,[‡,§] and Mercouri G. Kanatzidis*[,⊥]

[†]School of Materials Science and Engineering, Beihang University, Beijing 100191, China

[‡]Department of Physics and [§]Shenzhen Key Laboratory of Thermoelectric Materials, South University of Science and Technology of China, Shenzhen 518055, China

[⊥]Department of Chemistry, Northwestern University, Evanston, Illinois 60208, United States

[∥]Department of Physics, University of Michigan, Ann Arbor, Michigan 48109, United States

Supporting Information

ABSTRACT: We report enhanced thermoelectric performance in SnTe, where significantly improved electrical transport properties and reduced thermal conductivity were achieved simultaneously. The former was obtained from a larger hole Seebeck coefficient through Fermi level tuning by optimizing the carrier concentration with Ga, In, Bi, and Sb dopants, resulting in a power factor of 21 μW cm^{-1} K^{-2} and ZT of 0.9 at 823 K in $Sn_{0.97}Bi_{0.03}Te$. To reduce the lattice thermal conductivity without deteriorating the hole carrier mobility in $Sn_{0.97}Bi_{0.03}Te$, SrTe was chosen as the second phase to create strained endotaxial nanostructures as phonon scattering centers. As a result, the lattice thermal conductivity decreases strongly from ~2.0 Wm^{-1} K^{-1} for $Sn_{0.97}Bi_{0.03}Te$ to ~1.2 Wm^{-1} K^{-1} as the SrTe content is increased from 0 to 5.0% at room temperature and from ~1.1 to ~0.70 Wm^{-1} K^{-1} at 823 K. For the $Sn_{0.97}Bi_{0.03}Te$-3% SrTe sample, this leads to a ZT of 1.2 at 823 K and a high average ZT (for SnTe) of 0.7 in the temperature range of 300−823 K, suggesting that SnTe is a robust candidate for medium-temperature thermoelectric applications.

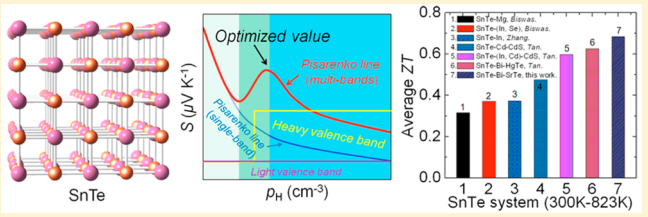

INTRODUCTION

Thermoelectric materials, capable of realizing the direct conversion between heat and electricity, have received worldwide attention in this era of energy shortage.[1−3] Most significant advances in the field of thermoelectrics have been achieved in lead chalcogenides,[4−7] in which very low thermal conductivity can be obtained via hierarchically all-scale phonon scattering[5] and high electrical transport properties through tuning its complex valence band structure.[6−8] In this context, attention has also turned recently to SnTe, which resembles PbTe[9−11] in many aspects (rock-salt crystal structure, small band gaps, complex valence band structure, etc.) but also has severe drawbacks that historically have made it an inferior thermoelectric material. For example, unlike PbTe, SnTe is intrinsically a heavily doped p-type semiconductor with a very high carrier concentration (~10^{21} cm^{-3}) that arises from an intrinsically large number of Sn vacancies.[12,13] Such high carrier concentration is difficult to control and results in low thermoelectric performance in pristine SnTe. The very high electrical conductivity (~7000 S cm^{-1}), but extremely low Seebeck coefficient (~20 μV K^{-1}), and high total thermal conductivity (~8.0 Wm^{-1} K^{-1} at room temperature) give a mediocre ZT (~0.2 at 723 K).[13] However, recent studies have unambiguously shown that SnTe has strong potential of being a promising thermoelectric material through band engineering and/or all-scale hierarchical architecturing.[14−23] Specifically, the Seebeck coefficient can be enhanced near room temperature through DOS distortion (In doping)[20] and above room temperature through valence band convergence (Cd, Hg, Mg, and Mn alloying) individually[6,15,16,19,24−27] or simultaneously in a broad temperature range through In/Cd codoping.[17] Besides, high-performance SnTe can also be achieved by reducing the thermal conductivity via all-scale phonon scattering, including atomic-scale alloying,[14,21,22] nanoscale grain[20] and phase interfaces,[23] and mesoscale grain boundaries.[14−19,21,22]

The existence of two valence bands in SnTe (as in PbTe) has already been confirmed, resulting in a unique Seebeck coefficient behavior as the carrier concentration is varied (Seebeck Pisarenko relation).[13] As shown in Figure 1a, the band gap of SnTe is about 0.18 eV at room temperature and the energy offsets between the light valence (L) band and the heavy valence (Σ) is about 0.40 eV. With the increase of carrier (hole) concentration, the Fermi level experiences three regions, from L band (region I), L band plus partial Σ band (region II), to L band plus Σ band (region III). Accordingly, the Seebeck

Received: December 19, 2015
Published: February 12, 2016

DOI: 10.1021/jacs.5b13276
J. Am. Chem. Soc. 2016, 138, 2366−2373

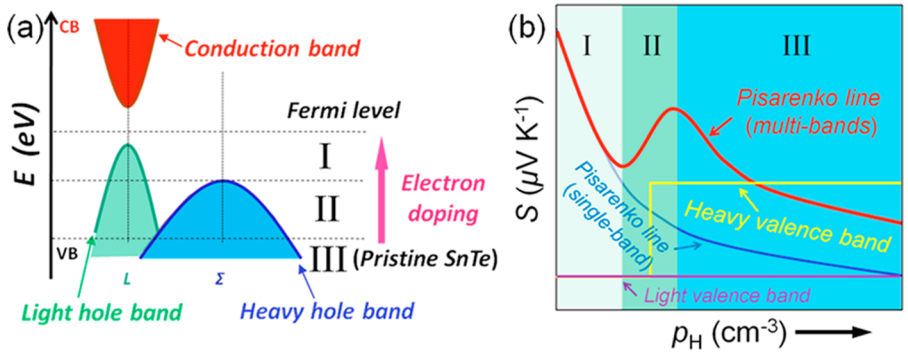

Figure 1. (a) Plot of the relative band energy for the conduction band (C), light valence band (L), and heavy valence band (Σ) of SnTe; schematic showing the Fermi level moving up with rising electron doping. (b) With increasing carrier concentration, the carrier transport experiences three regions: light valence band (region I), light valence band + parial heavy valence band (region II), and light valence band + heavy valence band (region III). The involvement of a heavy valence band causes a Pisarenko line upturn.

coefficient versus carrier concentration exhibits three typical regions (Figure 1b): an inverse relation at region I and region III; an accordant relation at region II, and a maximum close to region III.[13] It is indeed the enhanced effective hole masses (due to L and Σ band convergence) that result in the overall higher Seebeck coefficients than the calculation based on the single valence band (L), as shown in Figure 1b.[13] It is readily seen that the involvement of heavy valence band (Σ) causes an upturn in the Pisarenko line, which further indicates that the Seebeck coefficient can achieve a maximum at a given hole carrier concentration. The concept of valence band convergence in PbTe with rising temperature was recognized in early studies.[7,28−30] The intrinsic high hole carrier concentration (the Fermi level locates in region III) and relatively large valence band energy offset of SnTe, however, have been problematic in studying the same effect in these materials. The potential for counter (electron) doping or alloying to achieve valence band convergence, aiming to optimize the electrical transport properties, has not been explored to a significant extent.

In this study, we report that considerably enhanced thermoelectric performance can be achieved in SnTe using two successive approaches. First, to achieve large Seebeck coefficient, the electrical transport properties of SnTe were optimized by tuning the carrier concentration and Fermi level using electron doping with the electron donors Ga, In, Bi, and Sb. Second, using the electron-optimized SnTe, we employ SrTe as the second phase, which forms effective strained endotaxial nanostructures to reduce the thermal conductivity.[5,31] A high ZT of 1.2 at 823 K and a high average ZT of 0.7 in the 300−823 K range were achieved in the composition of $Sn_{0.97}Bi_{0.03}Te$-3% SrTe. Our results indicate that SnTe is a robust candidate for medium-temperature thermoelectric applications.

EXPERIMENTAL SECTION

Starting Materials. Reagent chemicals were used as obtained: Sn chunk (99.9999%, American Elements, USA), Te shot (99.999%, 5N Plus, Canada), Ga ingot (99.99%, American Elements, USA), In ingot (99.99%, American Elements, USA), Bi shot (99.999%, American Elements, USA), Sb shot (99.99%, Alfa, USA), and Sr chunk (99.99%, American Elements, USA).

Synthesis. High-purity single elements Sn, Ga, In, Bi, Sb, Sr, and Te were weighed according to the nominal compositions of $Sn_{1-x}Q_xTe$-y% SrTe (Q = Ga, In, Bi, Sb; x = 0, 0.01, 0.02, 0.03, 0.04, 0.05, and 0.06; y = 1, 2, 3, 4, 5; x and y are in mole ratio) and then put inside 13 mm diameter fused quartz tubes. The tubes were sealed under vacuum (~10^{-4} Torr) and slowly heated to 723 K in 12 h and then to 1423 K in 6 h, soaked at this temperature for 6 h, and subsequently cooled in a furnace to room temperature. The resultant ingots were crushed into fine powders and then densified by a spark plasma sintering (SPS) method (SPS-211LX, Fuji Electronic Industrial Co., Ltd.) at 923 K for 5 min in a 12.7 mm diameter graphite die under an axial compressive stress of 40 MPa in vacuum. Highly dense (>96% of theoretical density) disk-shaped pellets with dimensions of 12.7 mm in diameter and 9 mm in thickness were obtained.

Electrical Transport Properties. The obtained SPS-processed pellets were cut into bars with dimensions of 12 mm × 3 mm × 3 mm that were used for simultaneous measurement of the Seebeck coefficient and the electrical conductivity using an Ulvac Riko ZEM-3 instrument under a helium atmosphere from room temperature to 823 K. The samples were coated with a thin (~0.1−0.2 mm) layer of boron nitride (BN) to protect the instruments; please see previous report[39] for sample photographs and details for the BN coating process. Heating and cooling cycles gave repeatable electrical properties. Electrical properties obtained from different slices cut from the same pellets were similar, attesting to the homogeneity of the samples. The uncertainty of the Seebeck coefficient and electrical conductivity measurements is 3%.

Hall Measurements. The Hall coefficient was measured with a homemade high-temperature apparatus, which provides a working range from 300 to 823 K. The sample was press mounted and protected with argon gas to avoid possible oxidation at high temperature. The Hall resistance was monitored with a Linear Research AC resistance bridge (LR-700), with constant magnetic fields of ±1 T applied by using an Oxford superconducting magnet.

Thermal Conductivity. Highly dense SPS-processed pellets were cut and polished into a squared shape of 6 × 6 × 2 mm^3 for thermal diffusivity measurements. The samples were coated with a thin layer of graphite to minimize errors from the emissivity of the material. The thermal conductivity was calculated from $\kappa = D \times C_p \times \rho$, where the thermal diffusivity coefficient (D) was measured using the laser flash diffusivity method in a Netzsch LFA457, the specific heat capacity (C_p) was indirectly derived using a reference sample (Pyroceram 9606) in the range of 300−823 K, and the density (ρ) was determined using the dimensions and mass of the sample. The thermal diffusivity data were analyzed using a Cowan model with pulse correction. The uncertainty of the thermal conductivity is estimated to be within 10%, comprising uncertainties of 3% for the thermal diffusivity (D), 5% for the specific heat (C_p), and 2% for the sample density (ρ). The combined uncertainty for all measurements involved in the calculation of ZT is around 20%. Unless otherwise noted, all the properties described in this study were measured perpendicular to the sintering pressure direction, although no directional anisotropy effects were observed in the charge transport properties.

Electron Microscopy and X-ray Diffraction. Transmission electron microscopy (TEM) investigations were carried out in a FEI

DOI: 10.1021/jacs.5b13276
J. Am. Chem. Soc. 2016, 138, 2366−2373

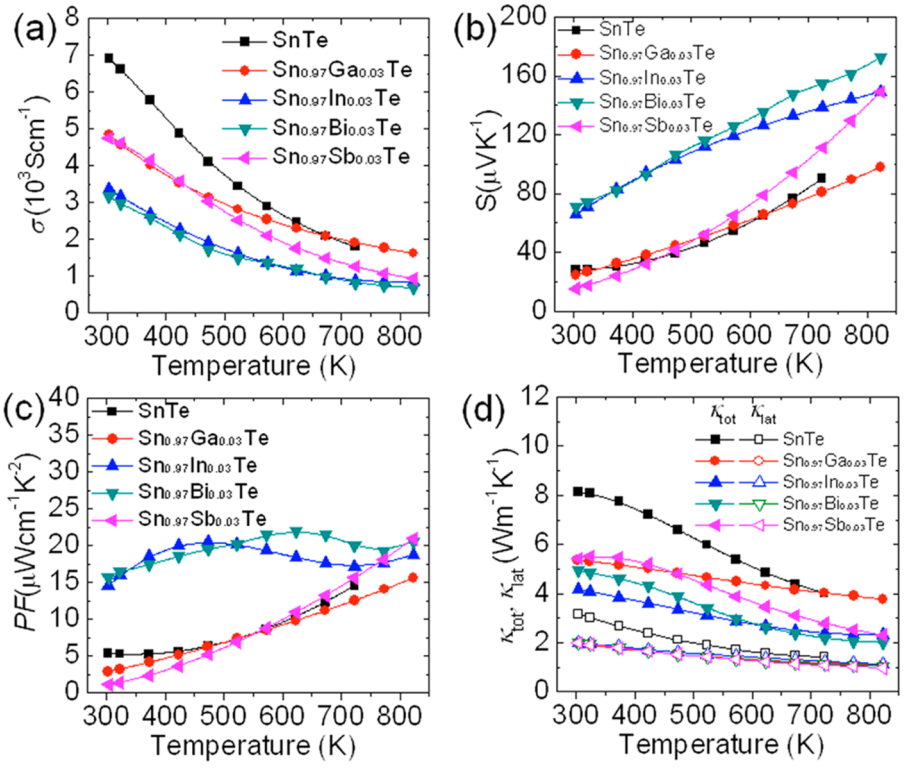

Figure 2. Thermoelectric properties as a function of temperature for pristine SnTe and $Sn_{0.97}M_{0.03}Te$ (M = Ga, In, Bi, and Sb): (a) electrical conductivity; (b) Seebeck coefficient; (c) power factor; (d) total and lattice thermal conductivities.

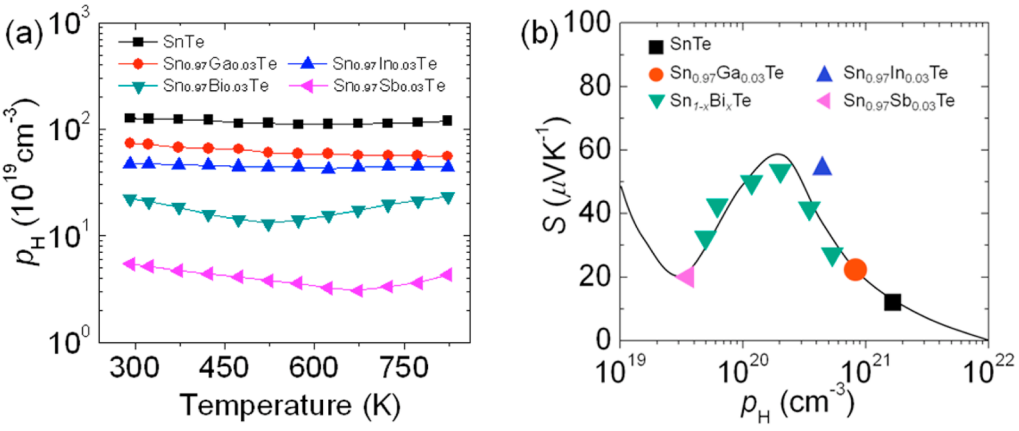

Figure 3. (a) Carrier concentrations as a function of temperature for pristine SnTe and $Sn_{0.97}M_{0.03}Te$ (M = Ga, In, Bi, and Sb). (b) Pisarenko line of SnTe and Seebeck coefficients of pristine SnTe and electron-doped SnTe.

Tecnai TF20 microscope operated at 200 kV. The thin TEM specimens were prepared by conventional methods, include cutting, grinding, polishing, dimpling, and Ar ion milling on a liquid nitrogen cooling stage. Samples pulverized with an agate mortar were used for powder X-ray diffraction. The powder diffraction patterns were obtained with Cu Kα (λ = 1.5418 Å) radiation in a reflection geometry on an Inel diffractometer operating at 40 kV and 20 mA and equipped with a position-sensitive detector.

RESULTS AND DISCUSSION

Optimizing Thermoelectric Properties of SnTe through Electron Doping. The Seebeck Pisarenko relation in Figure 1b indicates that the Seebeck coefficient could peak at an optimized carrier concentration.[13] The room temperature Seebeck coefficient of undoped SnTe is only +20 μV K^{-1} because of the intrinsically high hole carrier concentration

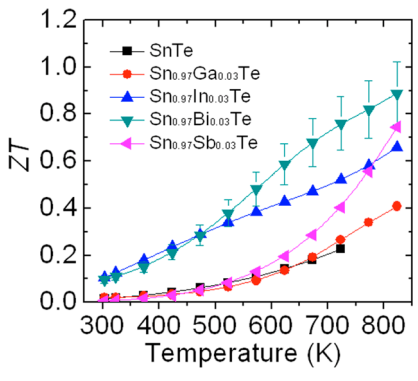

Figure 4. *ZT* values as a function of temperature for pristine SnTe and $Sn_{0.97}M_{0.03}Te$ (M = Ga, In, Bi, and Sb).

DOI: 10.1021/jacs.5b13276
J. Am. Chem. Soc. 2016, 138, 2366−2373

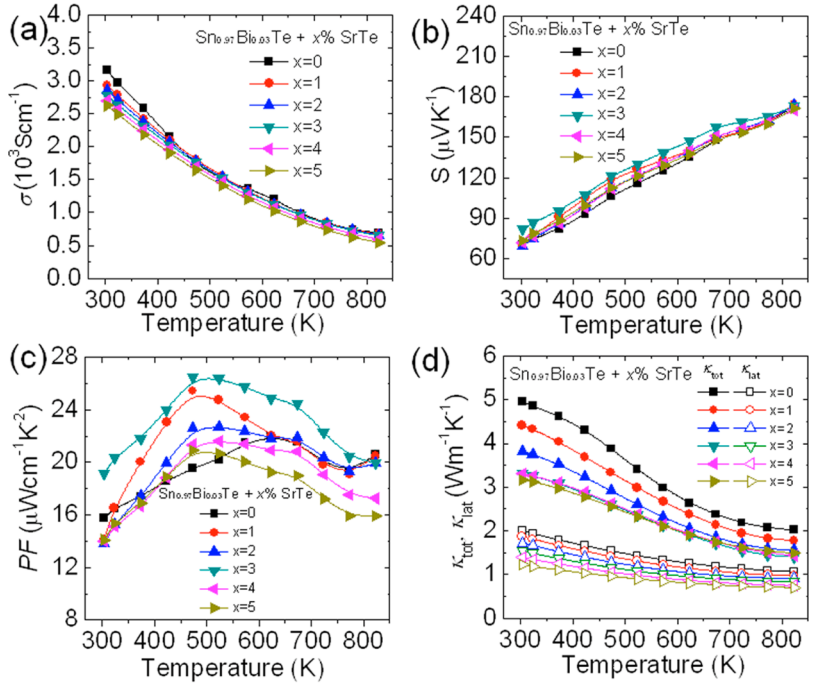

Figure 5. Thermoelectric properties as a function of temperature for $Sn_{0.97}Bi_{0.03}Te$-x% SrTe (x = 0, 1, 2, 3, 4, 5): (a) electrical conductivity; (b) Seebeck coefficient; (c) power factor; (d) total and lattice thermal conductivities.

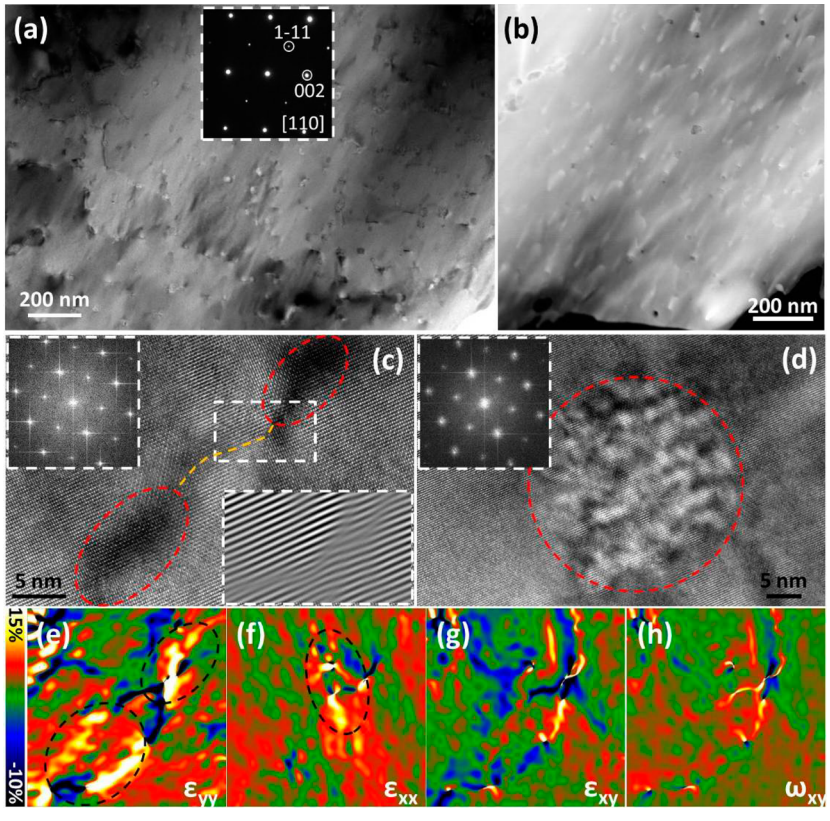

Figure 6. Microstructures of $Sn_{0.97}Bi_{0.03}Te$-3% SrTe: (a) Medium-magnification TEM and (b) HAADF images show the presence of nanoscale precipitates; the inset in (a) is the respective electron diffraction pattern along [111]. (c) HRTEM image focusing on two nanoscale precipitates with distorted connection between them; the top-left inset is the respective FFT image, and the bottom-right inset is the IFFT image showing lattice distortion between the two precipitates. (d) HRTEM image showing Moiré fringes, modulated by the overlapping between the precipitate and the matrix and the inset showing double diffraction pattern. (e–h) Strain maps (strain tensor ε_{yy}, ε_{xx}, ε_{xy}, and rotation ω_{xy}) reflect high strain states around the precipitates and the distortion connection between precipitates.

DOI: 10.1021/jacs.5b13276
J. Am. Chem. Soc. 2016, 138, 2366–2373

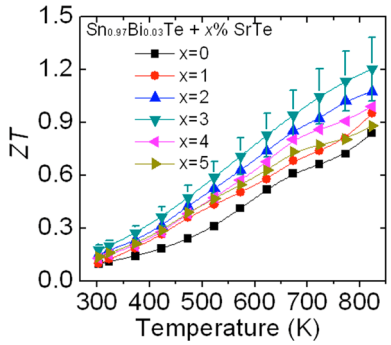

Figure 7. ZT values as a function of temperature for $Sn_{0.97}Bi_{0.03}Te$-x% SrTe (x = 0, 1, 2, 3, 4, 5).

($\sim 10^{21}$ cm^{-3}). To optimize the Seebeck coefficient, we chose Ga, In, Bi, and Sb as electron dopants (counter-doping) to reduce the hole concentration of SnTe. The XRD patterns in Figure S1 indicate that all $Sn_{1-x}M_xTe$ (M = Ga, In, Bi, and Sb; x = 0−0.06) are apparent single phases in the rock-salt SnTe structure. After electron counter-doping, the room temperature electrical conductivity of p-type SnTe is significantly reduced from ~7000 to 2000−3000 S cm^{-1} (Figure S2). To elucidate the doping effects of the different electron donor dopants (Ga, In, Bi, and Sb), we selected the 3% doping fraction for comparisons since the electrical transport properties were optimized and achieved at 3 mol %. Figure 2a shows that the electrical conductivity at room temperature was reduced from ~7000 to ~5000 S cm^{-1} for Ga- and Sb-doped SnTe and to ~3500 S cm^{-1} for In- and Bi-doped samples. Electron doping also has a strong effect on the Seebeck coefficient (Figure S3). The SnTe samples doped with In and Bi remain strongly p-type and have higher Seebeck coefficients than those doped with Ga and Sb. Specifically, at room temperature, the Seebeck coefficient is ~60 μV K^{-1} for 3% In- and Bi-doped samples and ~30 μV K^{-1} for 3% Ga- and Sb-doped samples (Figure 2b). For the In-doped sample, the higher Seebeck coefficient arises from the DOS distortion due to the formation of resonant levels in the valence band.[20] However, this enhancement just exists only around room temperature, which can be evidenced from the very close high-temperature Seebeck coefficients between In-doped and Bi/Sb-doped samples (Figure 2b). Unlike the In-doped sample, the higher Seebeck coefficient of the Bi-doped sample actually results from carrier concentration optimization (Figure 3). Namely, Bi doping reduced the hole carrier concentrations at room temperature from ~2 × 10^{21} to ~2 × 10^{20} cm^{-3} for SnTe, which corresponds to the Seebeck maximum indicated by the Pisarenko plot, as shown in Figure 3b. The optimized carrier concentrations give enhanced power factor plateaus over a broad temperature range, as shown in Figure 2c and Figure S4. The present results indicate that Bi doping enhances the Seebeck coefficient by tuning Fermi level via annihilating holes and reducing the hole carrier concentration. This mechanism is distinct from that of In, which enhances the room temperature Seebeck coefficient via resonance levels.[20]

The total thermal conductivity (κ_{tot}) shows a significant reduction with increasing doping content (Ga, In, Bi, and Sb), as the result of simultaneously reduced electronic and lattice thermal conductivity (Figure 2d). κ_{tot} is the sum of the electronic (κ_{ele}) and lattice thermal conductivity (κ_{lat}), $\kappa_{ele} = L\sigma T$, where L is the Lorenz number, which can be extracted based on fitting of the respective Seebeck coefficient values that estimate the reduced chemical potential (η).[32,33] Heat capacity, thermal diffusivity, Lorenz number, and electronic thermal conductivity values for $Sn_{1-x}M_xTe$ (M = Ga, In, Bi, and Sb; x = 0−0.06) are shown in Figures S5−S9. The lattice thermal conductivity, κ_{lat}, of SnTe is reduced presumably by point defect scattering through the electron dopants.[34,35] Indeed, a clear trend can be seen where the lattice thermal conductivity, κ_{lat}, decreases with increasing doping fraction for all dopants (Ga, In, Bi, and Sb). The dimensionless figure of merit (ZT) shows an increasing trend with temperature, and the maximum ZT value of 0.9 is achieved at 823 K for the $Sn_{0.97}Bi_{0.03}Te$ sample (Figure 4).

Enhancing Performance of $Sn_{0.97}Bi_{0.03}Te$ through Strained Endotaxial Nanostructuring with SrTe. We note that the lattice thermal conductivity, κ_{lat}, of $Sn_{0.97}Bi_{0.03}Te$ is still high; namely, it ranges from ~2.0 Wm^{-1} K^{-1} at room temperature to ~1.0 Wm^{-1} K^{-1} at 823 K, thus leaving room for a further κ_{lat} reduction to achieve even higher ZT values. In the lead and tin chalcogenides,[1,16−19,24] the lattice thermal conductivities can be significantly reduced by introducing endotaxial nanoprecipitates which do not deteriorate the charge carrier mobility severely if band-aligned.[36−39] In this study, we chose SrTe as the second phase to create nanostructures similar to the case in PbTe.[31] The thermoelectric properties of SnTe with varying amounts of SrTe (up to 5%) were evaluated in $Sn_{0.97}Bi_{0.03}Te$, as shown below.

The electrical conductivities decrease with increasing temperature and also with increasing amount of SrTe over the entire temperature range (Figure 5a); on the contrary, the Seebeck coefficients increase with rising temperature and are higher in SnTe samples with a larger amount of SrTe (Figure 5b), which is possibly from the valence band convergence through SrTe alloying in SnTe, as Mg in PbTe[38] and Mn in SnTe.[24] As shown in Figure 5c, the power factors for all samples peak at ~500 K and then decrease with rising temperature. The total thermal conductivity shows a significant decrease with increasing SrTe content (Figure 5d). Heat capacity, thermal diffusivity, Lorenz number, and electronic thermal conductivity for $Sn_{0.97}Bi_{0.03}Te$ with varying amounts of SrTe are given in Figure S11. A similar falling trend is also observed in the lattice thermal conductivity (Figure 5d), indicating that the dispersed SrTe phase is highly effective as a phonon scattering source. At room temperature, the lattice thermal conductivity decreases significantly from ~2.0 Wm^{-1} K^{-1} in $Sn_{0.97}Bi_{0.03}Te$ to ~1.5 Wm^{-1} K^{-1} in the $Sn_{0.97}Bi_{0.03}Te$ sample with 3.0% SrTe; this value further decreases to ~1.2 Wm^{-1} K^{-1} if the SrTe content is increased to 5.0%. Correspondingly, the lattice thermal conductivity at 823 K decreases from ~1.1 Wm^{-1} K^{-1} for $Sn_{0.97}Bi_{0.03}Te$ to ~0.8 and ~0.7 Wm^{-1} K^{-1} for samples with 3.0 and 5.0% SrTe, respectively.

The state of SrTe as the second phase in SnTe was evaluated by microstructural studies using analytical TEM. The medium-magnification bright-field TEM (BF-TEM) and high-angle annular dark-field (HAADF) images in Figure 6a,b present a consistently high density of nanoscale precipitates (5−20 nm in size) distributed evenly in the whole area. The Z-contrast feature of the HAADF imaging mode additionally reflects the composition difference between the precipitates and the SnTe matrix. The composition contrast can also be evidenced by the energy-dispersive X-ray spectroscopy (EDS) (Figure S12) obtained from the precipitates that exhibit characteristic peaks for Sr and Bi, which are not seen in the matrix. The high-

DOI: 10.1021/jacs.5b13276
J. Am. Chem. Soc. 2016, 138, 2366−2373

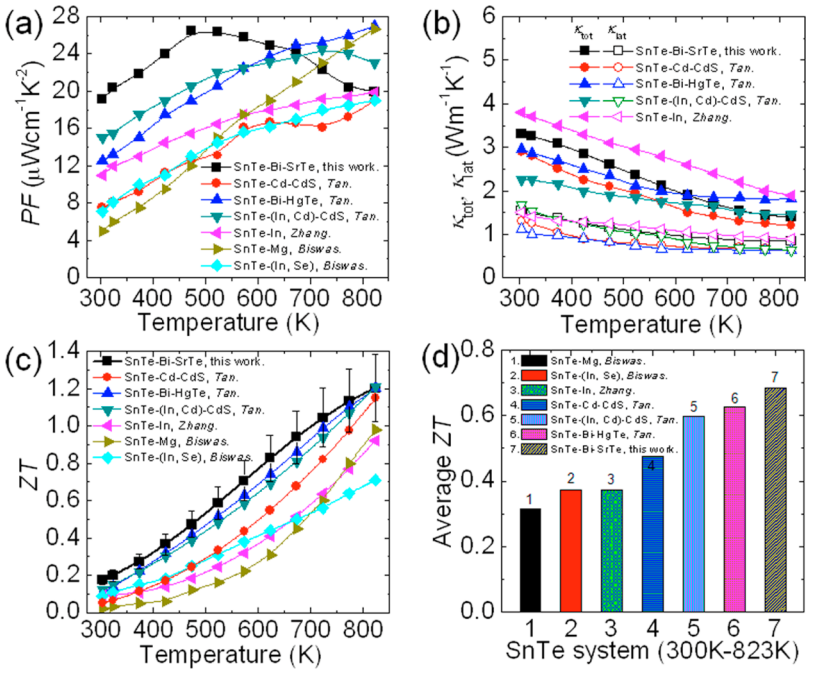

Figure 8. Thermoelectric property comparisons of $Sn_{0.97}Bi_{0.03}Te$-3% SrTe, Cd-doped SnTe-CdS,[19] Bi-doped SnTe-HgTe,[16] In/Cd-codoped SnTe-CdS,[17] In-doped SnTe,[20] Mg-doped SnTe,[15] and In/Se-codoped SnTe:[14] (a) power factor; (b) total and lattice thermal conductivities; (c) ZT values (the error bar of ZT is about 20%); (d) average ZT values.

resolution TEM (HRTEM) image in Figure 6c focuses on two precipitates, exhibiting a coherent interface with the matrix. Accordingly, the respective fast Fourier transformation (FFT) image (the top-left inset) shows no obvious peak splitting and reflects an endotaxial relationship between the two phases. The image also reveals a certain lattice distortion between the two precipitates, which is more obvious in the inverse FFT (IFFT) image (the top-left inset). To analyze the possible strain around the precipitates and the connection between them, high-quality HRTEM images were analyzed by geometric phase analysis,[40] which is a semiquantitative lattice image-processing approach for revealing spatial distribution of relative elastic strain. The strain state around the precipitates can be reflected in the ε_{yy} ($\varepsilon_{yy} = \partial u_y/\partial y$, where u is 2-D displacement) strain tensor map, while the distorted connection between the precipitates can be revealed in $\varepsilon_{xx}/\varepsilon_{xy}$ ($\varepsilon_{xx} = \partial u_x/\partial x$, $\varepsilon_{xy} = \frac{1}{2}\left(\frac{\partial u_y}{\partial x} + \frac{\partial u_x}{\partial y}\right)$) strain tensor or the ω_{xy} ($\omega_{xy} = \frac{1}{2}\left(\frac{\partial u_y}{\partial x} - \frac{\partial u_x}{\partial y}\right)$) rotation strain maps. The strain mainly occurs along certain directions, while it is relatively weak in other directions, as shown in Figure 6e,f.

These different strain states can provide an extensive scattering for phonons moving along different directions. The strain is mainly due to lattice or orientation mismatch between the matrix and the second phase. It is a pervasive defect effect associated with point defects, dislocations, and various interfaces. The high density of interface-induced elastic strain around nanoscale precipitates plays a significant role on affecting the phonon propagation pathways and thus achieving effective phonon scattering.[31] In addition, Moiré fringes can be found around the precipitate in the lattice image (Figure 6d); reciprocally, double diffraction can be observed in the diffraction pattern, as seen in the inset. It is well-known that Moiré fringes form by the interference between two sets of crystal planes with nearly common periodicity and/or small relative rotation angle.[41,42] Therefore, the introduction of Sr into Bi-doped SnTe could establish multiscale phonon scattering centers. Besides the mesoscale grains (not shown here), which can effect long-wavelength phonon scattering, nanoscale precipitates could effectively contribute in medium-wavelength phonon scattering. Furthermore, on the atomic scale, point defects and respective strain due to solid solution of Bi and Sr in the SnTe lattice could scatter short-wavelength phonon efficiently. These multiscale phonon scattering mechanisms collectively contribute to the very low lattice thermal conductivity in $Sn_{0.97}Bi_{0.03}Te$ samples with SrTe.

As shown in Figure 7, the ZT value climbs to ~1.2 at 823 K for the $Sn_{0.97}Bi_{0.03}Te$ sample with 3.0% SrTe yet shows no sign of saturation at higher temperatures. This value is 33% higher than the ZT value of 0.90 for the $Sn_{0.97}Bi_{0.03}Te$ sample without SrTe at the same temperature, indicating that the introduction of 3.0% SrTe significantly boosts the thermoelectric properties of p-type SnTe.

Compared with the previously reported SnTe systems, the power factors for $Sn_{0.97}Bi_{0.03}Te$-3.0% SrTe are higher at 300–650 K, which is due to the optimized electrical transport properties by tuning the carrier concentrations via electron doping (Figure 8a). Figure 8b shows that the total and lattice thermal conductivities are comparable in these SnTe systems. Figure 8c shows that the ZT values for $Sn_{0.97}Bi_{0.03}Te$-3.0% SrTe at 823 K are higher than that in other reported SnTe systems,[14−21] which is due to the improvement in power factor. We note that it is the ZT_{ave} (not ZT_{max}) over the entire working temperature range that defines the thermoelectric conversion efficiency.[43] The ZT_{ave} can be calculated by integrating the area under the ZT curve divided by the temperature difference based on the relationship $ZT_{ave} = \frac{1}{T_h - T_c}\int_{T_c}^{T_h} ZT\,dT$, where T_h and T_c are the hot-side and the cold-side temperatures, respectively. Therefore, it is useful to compare the various average ZT values of SnTe-based systems[14−21] (see Figure 8d). In the temper-

DOI: 10.1021/jacs.5b13276
J. Am. Chem. Soc. 2016, 138, 2366−2373

ature range of 300−823 K, the average ZT of our $Sn_{0.97}Bi_{0.03}Te$-3.0% SrTe sample is ∼0.7 and higher than that of all previously reported SnTe systems.

CONCLUDING REMARKS

We demonstrated that p-type SnTe can achieve a high ZT value of 1.2 at 823 K. The ZT trend is expected to continue past 900 K and reach 1.4 or even higher.[16,17,24,25] The high performance of SnTe was accomplished by optimizing the power factor (Seebeck coefficients) by tuning the carrier concentration with electron doping and combined with a simultaneous large reduction in the lattice thermal conductivity by introducing SrTe nanostructures. The observed promising thermoelectric properties indicate that SnTe is a robust thermoelectric material for high-temperature power generation applications.

ASSOCIATED CONTENT

Supporting Information

The Supporting Information is available free of charge on the ACS Publications website at DOI: 10.1021/jacs.5b13276.

Figures S1−S12 (PDF)

AUTHOR INFORMATION

Corresponding Authors

*zhaolidong@buaa.edu.cn

*m-kanatzidis@northwestern.edu

Present Address

#(Haijun Wu) Department of Materials Science and Engineering, National University of Singapore, 7 Engineering Drive 1, Singapore 117575.

Notes

The authors declare no competing financial interest.

ACKNOWLEDGMENTS

This work was supported in part by the Department of Energy, Office of Science Basic Energy Sciences Grant DE-SC0014520 (synthesis and characterization of samples). This work was also supported by the "Zhuoyue" Program from Beihang University, the Recruitment Program for Young Professionals, and the National Natural Science Foundation of China under Grant 51571007. This work was also partly supported by the Science, Technology and Innovation Commission of Shenzhen Municipality under Grant No. ZDSYS20141118160434515 and Guangdong Science and Technology Fund under Grant No. 2015A030308001 and the leading talents of Guangdong province Program. Microstructure characterization was performed in Center of Electron Microscopy in Zhejiang University.

REFERENCES

(1) (a) Zhao, L.-D.; Dravid, V. P.; Kanatzidis, M. G. *Energy Environ. Sci.* **2014**, *7*, 251. (b) Zhu, T. J.; Fu, C. G.; Xie, H. H.; Liu, Y. T.; Zhao, X. B. *Adv. Energy Mater.* **2015**, *5*, 1500588.

(2) (a) Minnich, A. J.; Dresselhaus, M. S.; Ren, Z. F.; Chen, G. *Energy Environ. Sci.* **2009**, *2*, 466. (b) Zhang, X.; Zhao, L.-D. *Journal of Materiomics* **2015**, *1*, 92.

(3) (a) Snyder, G. J.; Toberer, E. S. *Nat. Mater.* **2008**, *7*, 105. (b) Zhao, L.-D.; He, J. Q.; Berardan, D.; Lin, Y. H.; Li, J.-F.; Nan, C.-W.; Dragoe, N. *Energy Environ. Sci.* **2014**, *7*, 2900.

(4) Hsu, K. F.; Loo, S.; Guo, F.; Chen, W.; Dyck, J. S.; Uher, C.; Hogan, T.; Polychroniadis, E. K.; Kanatzidis, M. G. *Science* **2004**, *303*, 818.

(5) Biswas, K.; He, J. Q.; Blum, I. D.; Wu, C. I.; Hogan, T. P.; Seidman, D. N.; Dravid, V. P.; Kanatzidis, M. G. *Nature* **2012**, *489*, 414.

(6) Heremans, J. P.; Jovovic, V.; Toberer, E. S.; Saramat, A.; Kurosaki, K.; Charoenphakdee, A.; Yamanaka, S.; Snyder, G. J. *Science* **2008**, *321*, 554.

(7) (a) Pei, Y. Z.; Shi, X. Y.; LaLonde, A.; Wang, H.; Chen, L. D.; Snyder, G. J. *Nature* **2011**, *473*, 66. (b) Liu, W.; Tan, X. J.; Yin, K.; Liu, H. J.; Tang, X. F.; Shi, J.; Zhang, Q. J.; Uher, C. *Phys. Rev. Lett.* **2012**, *108*, 166601.

(8) Pei, Y. Z.; Wang, H.; Snyder, G. J. *Adv. Mater.* **2012**, *24*, 6125.

(9) Tan, Q.; Zhao, L. D.; Li, J. F.; Wu, C. F.; Wei, T. R.; Xing, Z. B.; Kanatzidis, M. G. *J. Mater. Chem. A* **2014**, *2*, 17302.

(10) Zhao, L. D.; Lo, S. H.; Zhang, Y. S.; Sun, H.; Tan, G. J.; Uher, C.; Wolverton, C.; Dravid, V. P.; Kanatzidis, M. G. *Nature* **2014**, *508*, 373.

(11) Chen, C. L.; Wang, H.; Chen, Y. Y.; Day, T.; Snyder, G. J. *J. Mater. Chem. A* **2014**, *2*, 11171.

(12) Masek, J.; Nuzhnyj, D. N. *Acta Phys. Polym., A* **1997**, *92*, 915.

(13) Brebrick, R. F.; Strauss, A. J. *Phys. Rev.* **1963**, *131*, 104.

(14) Banik, A.; Biswas, K. *J. Mater. Chem. A* **2014**, *2*, 9620.

(15) Banik, A.; Shenoy, U. S.; Anand, S.; Waghmare, U. V.; Biswas, K. *Chem. Mater.* **2015**, *27*, 581.

(16) Tan, G. J.; Shi, F. Y.; Doak, J. W.; Sun, H.; Zhao, L. D.; Wang, P. L.; Uher, C.; Wolverton, C.; Dravid, V. P.; Kanatzidis, M. G. *Energy Environ. Sci.* **2015**, *8*, 267.

(17) Tan, G. J.; Shi, F. Y.; Hao, S. Q.; Chi, H.; Zhao, L. D.; Uher, C.; Wolverton, C.; Dravid, V. P.; Kanatzidis, M. G. *J. Am. Chem. Soc.* **2015**, *137*, 5100.

(18) Tan, G. J.; Shi, F. Y.; Sun, H.; Zhao, L. D.; Uher, C.; Dravid, V. P.; Kanatzidis, M. G. *J. Mater. Chem. A* **2014**, *2*, 20849.

(19) Tan, G. J.; Zhao, L. D.; Shi, F. Y.; Doak, J. W.; Lo, S. H.; Sun, H.; Wolverton, C.; Dravid, V. P.; Uher, C.; Kanatzidis, M. G. *J. Am. Chem. Soc.* **2014**, *136*, 7006.

(20) Zhang, Q.; Liao, B. L.; Lan, Y. C.; Lukas, K.; Liu, W. S.; Esfarjani, K.; Opeil, C.; Broido, D.; Chen, G.; Ren, Z. F. *Proc. Natl. Acad. Sci. U. S. A.* **2013**, *110*, 13261.

(21) Zhou, M.; Gibbs, Z. M.; Wang, H.; Han, Y. M.; Xin, C. N.; Li, L. F.; Snyder, G. J. *Phys. Chem. Chem. Phys.* **2014**, *16*, 20741.

(22) Chen, Y.; Nielsen, M. D.; Gao, Y. B.; Zhu, T. J.; Zhao, X. B.; Heremans, J. P. *Adv. Energy Mater.* **2012**, *2*, 58.

(23) Han, M. K.; Androulakis, J.; Kim, S. J.; Kanatzidis, M. G. *Adv. Energy Mater.* **2012**, *2*, 157.

(24) Tan, G. J.; Shi, F. Y.; Hao, S. Q.; Chi, H.; Bailey, T. P.; Zhao, L. D.; Uher, C.; Wolverton, C.; Dravid, V. P.; Kanatzidis, M. G. *J. Am. Chem. Soc.* **2015**, *137*, 11507.

(25) Wu, H. J.; Chang, C.; Feng, D.; Xiao, Y.; Zhang, X.; Pei, Y. L.; Zheng, L.; Wu, D.; Gong, S. K.; Chen, Y.; He, J. Q.; Kanatzidis, M. G.; Zhao, L. D. *Energy Environ. Sci.* **2015**, *8*, 3298.

(26) He, J.; Tan, X. J.; Xu, J. T.; Liu, G. Q.; Shao, H. Z.; Fu, Y. J.; Wang, X.; Liu, Z.; Xu, J. Q.; Jiang, H. C.; Jiang, J. *J. Mater. Chem. A* **2015**, *3*, 19974.

(27) Li, W.; Chen, Z.; Lin, S.; Chang, Y.; Ge, B.; Chen, Y.; Pei, Y. *Journal of Materiomics* **2015**, *1*, 307.

(28) Pei, Y.; Wang, H.; Snyder, G. J. *Adv. Mater.* **2012**, *24*, 6125.

(29) Pei, Y.; Wang, H.; Gibbs, Z. M.; LaLonde, A. D.; Snyder, G. J. *NPG Asia Mater.* **2012**, *4*, e28.

(30) Pei, Y.; LaLonde, A. D.; Heinz, N. A.; Shi, X.; Iwanaga, S.; Wang, H.; Chen, L.; Snyder, G. J. *Adv. Mater.* **2011**, *23*, 5674.

(31) Biswas, K.; He, J. Q.; Zhang, Q. C.; Wang, G. Y.; Uher, C.; Dravid, V. P.; Kanatzidis, M. G. *Nat. Chem.* **2011**, *3*, 160.

(32) Zhao, L. D.; Lo, S. H.; He, J. Q.; Li, H.; Biswas, K.; Androulakis, J.; Wu, C. I.; Hogan, T. P.; Chung, D. Y.; Dravid, V. P.; Kanatzidis, M. G. *J. Am. Chem. Soc.* **2011**, *133*, 20476.

(33) Liu, W. S.; Lukas, K. C.; McEnaney, K.; Lee, S.; Zhang, Q.; Opeil, C. P.; Chen, G.; Ren, Z. F. *Energy Environ. Sci.* **2013**, *6*, 552.

(34) Pei, Y. L.; He, J. Q.; Li, J. F.; Li, F.; Liu, Q. J.; Pan, W.; Barreteau, C.; Berardan, D.; Dragoe, N.; Zhao, L. D. *NPG Asia Mater.* **2013**, *5*, e47.

DOI: 10.1021/jacs.5b13276
J. Am. Chem. Soc. 2016, 138, 2366−2373

(35) Wan, C. L.; Pan, W.; Xu, Q.; Qin, Y. X.; Wang, J. D.; Qu, Z. X.; Fang, M. H. *Phys. Rev. B: Condens. Matter Mater. Phys.* **2006**, *74*, 144109.
(36) Lee, Y.; Lo, S. H.; Androulakis, J.; Wu, C. I.; Zhao, L. D.; Chung, D. Y.; Hogan, T. P.; Dravid, V. P.; Kanatzidis, M. G. *J. Am. Chem. Soc.* **2013**, *135*, 5152.
(37) Zhao, L. D.; He, J. Q.; Hao, S. Q.; Wu, C. I.; Hogan, T. P.; Wolverton, C.; Dravid, V. P.; Kanatzidis, M. G. *J. Am. Chem. Soc.* **2012**, *134*, 16327.
(38) Zhao, L. D.; Wu, H. J.; Hao, S. Q.; Wu, C. I.; Zhou, X. Y.; Biswas, K.; He, J. Q.; Hogan, T. P.; Uher, C.; Wolverton, C.; Dravid, V. P.; Kanatzidis, M. G. *Energy Environ. Sci.* **2013**, *6*, 3346.
(39) Zhao, L. D.; He, J. Q.; Wu, C. I.; Hogan, T. P.; Zhou, X. Y.; Uher, C.; Dravid, V. P.; Kanatzidis, M. G. *J. Am. Chem. Soc.* **2012**, *134*, 7902.
(40) Hytch, M. J.; Snoeck, E.; Kilaas, R. *Ultramicroscopy* **1998**, *74*, 131.
(41) Lo, S. H.; He, J. Q.; Biswas, K.; Kanatzidis, M. G.; Dravid, V. P. *Adv. Funct. Mater.* **2012**, *22*, 5175.
(42) Wu, H. J.; Carrete, J.; Zhang, Z. Y.; Qu, Y. Q.; Shen, X. T.; Wang, Z.; Zhao, L. D.; He, J. Q. *NPG Asia Mater.* **2014**, *6*, e108.
(43) Zhao, L.-D.; Tan, G.; Hao, S.; He, J.; Pei, Y.; Chi, H.; Wang, H.; Gong, S.; Xu, H.; Dravid, V. P.; Uher, C.; Snyder, G. J.; Wolverton, C.; Kanatzidis, M. G. *Science* **2016**, *351*, 141.

DOI: 10.1021/jacs.5b13276
J. Am. Chem. Soc. 2016, 138, 2366−2373